An adaptive L^p-penalization method to enhance the spatial resolution of microwave radiometer measurements

Matteo Alparone, *Student Member, IEEE,* Ferdinando Nunziata, *Senior Member, IEEE,*
Claudio Estatico, Flavia Lenti, and Maurizio Migliaccio, *Fellow Member, IEEE*

Abstract—In this paper we introduce a novel approach to enhance the spatial resolution of single-pass microwave data collected by meso-scale sensors. The proposed rationale is based on an L^p-minimization approach with a variable p exponent. The algorithm automatically adapts the p exponent to the region of the image to be reconstructed. This approach allows taking benefit of the advantages of both the regularization in Hilbert ($p = 2$) and Banach ($1 < p < 2$) spaces. Experiments are undertaken considering the microwave radiometer and refer to both actual and simulated data collected by the Special Sensor Microwave Imager (SSM/I). Results demonstrate the benefits of the proposed method in reconstructing abrupt discontinuities and smooth gradients with respect to conventional approaches in Hilbert or Banach spaces.

Index Terms—Resolution enhancement, inverse problem, microwave radiomenter.

I. INTRODUCTION

The microwave radiometer (MWR) is a passive remote sensing instrument whose measurements are related to the natural emission from the observed scene. MWR is a very important sensor for global monitoring of environmental parameters due to its dense revisit time associated with all-day and all-weather observation capabilities. Over the past few decades, a number of operational satellites equipped with MWRs have been launched for earth observation purposes. Among them, one can distinguish multi-frequency radiometers, e.g. Special Sensor Microwave Imager (SSM/I), Special Sensor Microwave Imager Sounder (SSMIS), Advanced Microwave Scanning Radiometer - EOS (AMSR-E), Advanced Microwave Scanning Radiometer 2 (AMSR2), Microwave Radiation Imager (MWRI) and single-frequency radiometers, e.g., Soil Moisture Active Passive (SMAP) radiometer and the Microwave Imaging Radiometer using Aperture Synthesis (MIRAS) operated by the European Space Agency (ESA) Soil Moisture and Ocean Salinity (SMOS) mission. MWR measurements are generally available into two formats: swath and gridded measurements. The former one consists of the irregularly sampled brightness temperature measurements; while the latter is obtained converting swath-based measurements into brightness temperature at fixed gridded locations [1]. Gridded products are of paramount importance when dealing with applications that rely on the analysis of parameters extracted at fixed location through time. A straightforward approach to generate gridded products consists of the conventional drop-in-the-bucket (DIB) method or weighted averaging based on the squared inverse distance [2], [3]. Those methods provide a gridded product whose spatial resolution is rather coarse (e.g., 25 km [3]).

Nowadays, there is an increasing interest towards gridded products at enhanced spatial resolution for a broad range of applications. Operational methods have been proposed that consist of either augmenting radiometer measurements with complementary observations [4] or reconstructing the brightness field on a finer resolution grid using image reconstruction methods that rely on the knowledge of the antenna pattern [5]–[11]. The first class of methods includes approaches based on the combination of MWR measurements with radar observations (e.g. [12]) and optical measurements (e.g. [13]). In [14] an approach based on the combination of measurements collected by the low- and high-frequency channels of a multi-frequency radiometer was proposed that is based on the Smoothing Filter-based Image Modulation technique (SFIM). According to methods based on image reconstruction approaches, resolution enhancement is possible due to the oversampling that characterizes the measurement process, i.e., radiometer measurements are

M. Alparone, F. Nunziata and M. Migliaccio are with the Dipartimento di Ingegneria, Università degli Studi di Napoli Parthenope, 80143 Napoli, Italy (e-mail: matteo.alparone@uniparthenope.it; ferdinando.nunziata@uniparthenope.it; maurizio.migliaccio@uniparthenope.it).

C. Estatico is with the Dipartimento di Matematica, Università degli Studi di Genova, 16146 Genova, Italy (e-mail: estatico@dima.unige.it). The work of Claudio Estatico is partially supported by GNCS-INDAM, Italy

F. Lenti is with the CLC Space GmbH, 64665 Alsbach-Hähnlein, Deutschland.

not independent from each other since adjacent beams are generally partially overlapped [8]. It is worth noting that the improved spatial resolution is obtained at the expense of a larger noise level [15]. This means that a tradeoff between resolution enhancement and noise amplification is due.

In this study a new reconstruction approach is proposed to enhance the spatial resolution of MWR measurements. In literature, the reference reconstruction method is the Backus-Gilbert (BG) technique [16] commonly used, for instance, to generate the SMAP Level 2 Enhanced Passive Soil Moisture product where the moisture map is provided on a 9 km spatial grid, instead of the conventional 36 km grid that characterizes the Level 2 SMAP soil moisture product [17]. In addition to BG method, a reconstruction algorithm based on the radiometer version of the Scatterometer Image Reconstruction (SIR) method [8] has been successfully applied to SMMR, SSM/I and AMSR-E measurements [18] and it is shown to provide performances similar to BG while improving the processing time and noise propagation (when multiple passes are used). Both BG and SIR are used to generate gridded radiometer products at both low and enhanced spatial resolution in the frame of the NASA-sponsored MEaSUREs programme [19].

In addition to these two reference methods, other image reconstruction approaches have been developed to enhance the spatial resolution of radiometer measurements that are based on the minimization of the L^p norm of the residual with $p = 2$, which is the classical least square minimization approach. This means that the reconstruction is addressed in a Hilbert space. Among these methods, it is worth mentioning the approaches based on the Truncated Singular Value Decomposition (TSVD) [9], [11] that is shown to outperform the BG method, the approaches based on the Tikhonov regularization [10], [20] and iterative methods based on gradient-like kernels [21]. Although Hilbert-space reconstructions provide satisfactory results when dealing with the reconstruction of gradients and, in general, signals resulting from phenomena that do not call for abrupt discontinuities, the main drawbacks are related to over smoothness and Gibbs-related oscillations that appear in presence of abrupt discontinuities [22].

Recently, reconstruction techniques in Banach spaces have been proposed that aim at minimizing the L^p-norm of the residual [21], [23], [24]. Reconstructions in Banach spaces are shown to be very promising since they allow overcoming drawbacks of classical Hilbert-space reconstructions, i.e., over smoothness and Gibbs oscillations. The key problem of Banach-space reconstructions relies on the choice of the optimal $1 < p < 2$. Theoretical and experimental analyses suggest p values

close to 1 to obtain remarkable reconstructions of abrupt discontinuities, e.g., sea/land edges etc. [23]. However, this choice will result in fictitious oscillations over areas where the background is not properly subtracted. In fact, the subtraction of the background, which is an important step when dealing with image reconstruction methods, it is even more important when the problem is addressed in Banach spaces, since it increases sparsity and reduces ringing effects. [15].

In this study, a single-pass spatial resolution enhancement method is proposed that aims at bridging the gap between reconstructions undertaken in Banach and Hilbert spaces. This is achieved by addressing the reconstruction in the L^p space with an adaptive p exponent that spans in the range $1.2 \leq p \leq 2$. This approach is expected to result in reconstructions that share the benefits of Hilbert and Banach spaces, while mitigating their drawbacks. In particular, the exponent is forced to be close to 1.2 (which was found to be a good compromise between sparsity and reliability of reconstruction in [23]) in the presence of abrupt discontinuities, while a p exponent that tends to 2 is adopted when areas with smooth gradients are to be reconstructed.

This paper is organized as follows: in Section II, after a brief review of resolution enhancement methods in classical Hilbert and Banach spaces, we describe the generalization to variable exponent Lebesgue spaces. In Section III, we present numerical results obtained by applying the proposed algorithm to both simulated and actual microwave radiometer measurements, while conclusions are shown in Section IV.

II. THEORETICAL BACKGROUND

In this section, after a brief primer on the reconstruction in Hilbert and Banach spaces, the adaptive L^p reconstruction method, with a variable p exponent is described.

The general MWR measurement, neglecting atmospheric effects, can be modeled as the surface brightness temperature $T_b(\theta, \phi)$ weighted by the antenna pattern $G_i(\theta, \phi)$. In particular, the single t-th measurement, denoted as the antenna temperature T_{A_t}, can be written as:

$$T_{A_t} = \bar{G}_t^{-1} \int \int G_t(\theta, \phi) T_b(\theta, \phi) d\theta d\phi \quad , \quad (1)$$

where

$$\bar{G}_t^{-1} = \int \int G_t(\theta, \phi) d\theta d\phi \quad . \quad (2)$$

Eq. (1) is a Fredholm integral equation of the first kind with a smooth kernel; hence it represents a linear

problem that, after discretization, can be cast in matricial form [11] as

$$A\mathbf{x} = \mathbf{b} \quad , \qquad (3)$$

where A is the matrix containing the projected antenna patterns related to the radiometer measurements, the unknown vector $\mathbf{x}$ stands for the brightness temperature T_B and $\mathbf{b}$ is the measurement vector. Since we aim at reconstructing the signal on a finer resolution grid (i.e., spatial resolution enhancement), $\mathbf{x} \in \mathbb{R}^m$ and $\mathbf{b} \in \mathbb{R}^n$ with $m > n$.

To perform spatial resolution enhancement, the ill-conditioned and undetermined linear problem (3) is to be solved [25]. The ill-conditioning, which is physically due to the fact that the direct operator (1) is a Fredholm integral with a smooth kernel, implies that a small error in the data can result in extremely large errors in the reconstructed field. Therefore, regularization methods must be invoked to reduce noise amplification and to obtain a reasonable approximation of the solution. In this study, the simplest iterative method, i.e. the gradient (also known as Landweber) regularization method is used. Moreover, the reconstruction of the brightness field on a finer spatial grid makes the problem (3) underdetermined. Hence, in order to invert the system, constraints on the signal to be reconstructed must be imposed. In this study, the adopted constraint consists of searching the minimum norm solution; hence, we first review the L^p-norm minimization with $p = 2$ (Hilbert spaces) and $p = 1.2$ (Banach spaces). Then, the novel minimization approach that is based on L^p spaces with a variable p exponent, will be described.

A. Iterative regularization in Hilbert and Banach spaces

When dealing with regularization in Hilbert spaces, the 2-norm of the residual $A\mathbf{x} - \mathbf{b}$ must be minimized. This corresponds to minimizing the following least square functional:

$$\Omega_2 = \frac{1}{2}||A\mathbf{x} - \mathbf{b}||_2^2 = \frac{1}{2}\sum_{i=1}^{n}(A\mathbf{x} - \mathbf{b})_i^2 \quad . \qquad (4)$$

This minimization can be straightforwardly obtained with the conventional gradient method, whose k-th iteration $\mathbf{x}_k$ is given by:

$$\mathbf{x}_k = \mathbf{x}_{k-1} - \lambda_k \nabla \Omega_2(\mathbf{x}_{k-1}) \quad , \qquad (5)$$

where λ_k is the step-size of the iteration. Considering that $\nabla\Omega_2(\mathbf{x}) = A^*(A\mathbf{x} - \mathbf{b})$, equation (5) becomes:

$$\mathbf{x}_k = \mathbf{x}_{k-1} - \lambda_k A^*(A\mathbf{x} - \mathbf{b}) \quad . \qquad (6)$$

It can be shown [26], [27] that (6) represents a regularization scheme whose regularization parameter is the number of iterations k. Regarding the step-size λ_k, an optimal choice is possible [23]:

$$\lambda_k = \lambda = \frac{1}{||A^*A||} \quad , \qquad (7)$$

which leads to the well known Landweber method in Hilbert spaces.

When moving from Hilbert to Banach spaces, the functional to be minimized becomes:

$$\Omega_p = \frac{1}{p}||A\mathbf{x} - \mathbf{b}||_p^p = \frac{1}{p}\sum_{i=1}^{n}(A\mathbf{x} - \mathbf{b})_i^p \quad . \qquad (8)$$

From a theoretical viewpoint, the iterative scheme (6) is not well-defined in L^p Banach space, since the operator A^* cannot be applied to the residual $A\mathbf{x} - \mathbf{b}$ [11], [28]. More specifically, $A\mathbf{x} - \mathbf{b}$ belongs to L^p space and A^* acts to its dual space $(L^p)^* = L^q$, for $p > 1$, where q is the Hölder conjugate of p (i.e. $\frac{1}{p} + \frac{1}{q} = 1$).

To overcome this issue, the so-called duality maps are introduced to link the elements of a Banach space with the elements of its dual space [29]. In this study, the following duality maps are used:

$$\begin{aligned} \mathcal{J}_p : L^p \to L^q \\ \mathcal{J}_q : L^q \to L^p \end{aligned} \quad , \qquad (9)$$

where:

$$\mathcal{J}_p(\mathbf{x})_i = |x_i|^{p-1}sign(x_i), \quad i = 1, \dots, m \quad , \qquad (10)$$

with $sign(\cdot)$ being the sign function. Hence, using (9) the k-th iteration of the Landweber method in the Banach spaces can be written as follows [28]:

$$\mathbf{x}_{k+1} = \mathcal{J}_q(\mathcal{J}_p(\mathbf{x}_k) - \lambda_k A^* \mathcal{J}_p(A\mathbf{x}_k - \mathbf{b})) \quad . \qquad (11)$$

Unfortunately, in Banach spaces there is no formula to set the optimal step size λ_k. However the Landweber method has been proved to converge in [28].

B. Iterative regularization in variable exponent Lebesgue spaces

In the case that the p exponent is no longer forced to be a fixed value, the minimization is to be performed in Lebesgue spaces with variable exponent L^p, i.e., the exponent p is a function $p(t) : \Omega \to [1, \infty]$ [30]. This corresponds to fix a constraint that consists of choosing the unique solution that minimizes $||\mathbf{x}||_{p(\cdot)}$

with a variable exponent $p(\cdot)$ [28], [30]. To formulate a gradient-like regularization scheme whose k-th iteration mimics equation (11), a key issue must be addressed that relies on the definition and the computation of the norm.

We recall that in the constant p exponent case, the p-norm is defined as:

$$||\mathbf{x}||_p = \sqrt[p]{\sum_{i=1}^{N} |x_i|^p} \qquad (12)$$

When the exponent p is not constant, the p-th root extraction, which is necessary to satisfy the homogeneity condition in the definition of the norm, is no longer defined. To overcome this issue, the adopted strategy consists of evaluating the argument of the p-th root, i.e. the so-called modulus:

$$\rho(\mathbf{x}) = \sum_{i=1}^{N} |x_i|^{p_i} \qquad . \qquad (13)$$

In this case, the variable p case is a straightforward generalization of the constant exponent case. Then, the so-called Luxemburg norm [30] is used, which can be calculated by solving the following minimization problem:

$$||\mathbf{x}||_{L^{p(\cdot)}} = \inf \left\{ \lambda > 0 : \rho \left(\frac{\mathbf{x}}{\lambda} \right) \leq 1 \right\} \qquad . \qquad (14)$$

Once the modulus and the Luxembourg norm are defined, the residual $\Omega_{p(\cdot)}$ becomes:

$$\Omega_{p(\cdot)} = ||A\mathbf{x} - \mathbf{b}||_{L^{p(\cdot)}} \qquad , \qquad (15)$$

where the scale factor $1/p$, which appears in the constant case (8), can be straightforwardly omitted without affecting the result. To minimize the residual, the Landweber iterative scheme is used. However, even in the variable p exponent case, the generic iteration exhibits the same problem of eq. (6) in the Banach space, since the subtraction is not well-defined. This implies that duality maps must be used. To generalize the duality map to the variable p exponent case, the seminal guideline provided in [31] is followed. Hence, the variable-p case duality map $\mathcal{J}_{L^{p(\cdot)}}(\mathbf{x})$ is a vector whose i-th component is given by:

$$(\mathcal{J}_{L^{p(\cdot)}}(\mathbf{x}))_i = \frac{p_i |x_i|^{p_i - 1} \text{sign}(x_i)}{||\mathbf{x}||_{p(\cdot)}^{p_i - c} \sum_{k=1}^{m} \frac{p_k |x_k|^{p_k}}{||\mathbf{x}||_{p(\cdot)}^{p_k}}} \qquad i = 1, \ldots, m \qquad (16)$$

where the constant $c > 1$ just acts as a scalar factor, since $||\mathbf{x}||^c$ is constant for all the i-th entries of $\mathcal{J}_{L^{p(\cdot)}}(\mathbf{x})$. Note

that the duality map (16) reduces to (10) when p is no longer variable and $c = p$.

Once the norm and the duality map have been generalized to the variable p exponent case, the k-th iteration of the Landweber in the $L^{p(\cdot)}$ spaces can be written as:

$$\mathbf{x}_{k+1} = \mathcal{J}_{L^{q(\cdot)}}\left(\mathcal{J}_{L^{p(\cdot)}}(\mathbf{x}_k) - \lambda_k A^* \mathcal{J}_r (A\mathbf{x}_k - \mathbf{b})\right) \quad , \quad (17)$$

where:

$$\begin{aligned} \mathcal{J}_{L^{p(\cdot)}} &: L^{p(\cdot)}(\mathbb{R}^m) \to \left(L^{p(\cdot)}(\mathbb{R}^m)\right)^* \\ \mathcal{J}_{L^{q(\cdot)}} &: L^{q(\cdot)}(\mathbb{R}^m) \to \left(L^{q(\cdot)}(\mathbb{R}^m)\right)^* \end{aligned} \quad , \quad (18)$$

are the duality maps with vectorial exponent, defined in accordance to (16), with $q(\cdot)$ being the vector Holder coniugate of $p(\cdot)$, that is, $\frac{1}{p_i} + \frac{1}{q_i} = 1$ for any element $i = 1, \ldots, m$. It is interesting to note that, unlike the constant exponent case of [28], the duality map $\mathcal{J}_{L^{q(\cdot)}}$ is not the inverse of the duality map $\mathcal{J}_{L^{p(\cdot)}}$, but rather it is only an approximation. The iteration scheme is well defined due to the isomorphism between $\left(L^{(\cdot)}(\mathbb{R}^m)\right)^*$ and $L^{q(\cdot)}(\mathbb{R}^m)$ [30].

Since for a dimensional issue the maps (18) cannot be applied to the term $A\mathbf{x}_k - \mathbf{b}$ (which belongs to the $\mathbb{R}^n$ space) the following duality map

$$\mathcal{J}_r : L^r(\mathbb{R}^n) \to L^s(\mathbb{R}^n) \qquad (19)$$

has been defined in accordance to (10), with $\frac{1}{r} + \frac{1}{s} = 1$. Since this map has a scalar exponent, a key issue consists of selecting it in a way that is linked to the variable exponent $p(\cdot)$. Hence, at any iteration k, we search for a scalar value r_k such that

$$||\mathbf{x}_k||_{L^{p(\cdot)}} = [\rho(\mathbf{x}_k)]^{\frac{1}{r_k}} \qquad . \qquad (20)$$

By taking the logarithm on both the sides one obtains:

$$\frac{1}{r_k} \ln(\rho(\mathbf{x}_k)) = \ln(||\mathbf{x}_k||_{p(\cdot)}) \qquad , \qquad (21)$$

which leads to:

$$r_k = \frac{\ln(\rho(\mathbf{x}_k))}{\ln(||\mathbf{x}_k||_{p(\cdot)})} \qquad , \qquad (22)$$

where $\rho(\mathbf{x}_k)$ is the modulus (13) and the norm $||\cdot||_{p(\cdot)}$ is computed according to (14).

To apply the proposed approach, the values assumed by the variable p exponent need to be specified. In this study, we force p to vary in the $[1.2, 2]$ interval. The extrema of this range of values correspond to: a) the well-known L^2 norm, which guarantees stable and accurate enough reconstructions when gradient-like discontinuities are in place; b) the $L^{1.2}$ norm, which has

been shown in [21] to represent the best compromise between reconstruction performance and algorithm stability when Banach spaces are considered. Note that, the value $p = 1$ cannot be used in our scheme, since the adopted duality maps are not well defined for $p = 1$. In addition, it is worth to point out that minimization in L^1 Banach spaces performs badly when the reference signal is not sparse enough., as in our numerical case [21]. Once the range of admissible p values has been selected, the rule that allows updating the k-th $p(\cdot)$ vector must be defined. In this study, a simple linear updating scheme is adopted:

$$p(\cdot)_i = p_{min} + \frac{p_{max} - p_{min}}{M - m}(x_i - m) \quad , \qquad (23)$$

where $m = \min(x)$, $M = \max(x)$, $p_{min} = 1.2$, $p_{max} = 2$. This updating function makes the $p(\cdot)$ vector a rescaled version of $\mathbf{x}$ in the interval [1.2,2].

The proposed approach is based on an iterative regularization algorithm whose regularization parameter is represented by the iteration number k. Hence, the choice of k at which the method has to be stopped is a crucial step to achieve a successful reconstruction. In this work we stop the iterations as soon as the residual stops to decrease in a stable way (i.e., it becomes flat or, surprisingly enough, even starts to increase). This very simple strategy that, although not theoretically proved, has been validated using the discrepancy principle [23].

III. NUMERICAL RESULTS

In this section, the performance of the adaptive L^p approach is contrasted with reference $p = 2$ (Hilbert), and $p = 1.2$ (Banach) reconstructions schemes. Experiments refer to both simulated and actual Special Sensor Microwave Imager (SSM/I) radiometer measurements. The latter is a seven-channel, four-frequency, linearly polarized radiometer that flew aboard the United States Defense Meteorological Satellite Program. SSM/I collects both horizontally and vertically polarized radiation at 19.35, 37.0 and 85.5 GHz and vertical only at 22.2 GHz [32]. In this study, reference is made to the lowest spatial resolution channel, i.e. the 19.35 GHz channel. The SSM/I nominal swath width covers about 1400 km, which results in an almost complete global coverage in 24 h [32]. It performs 64 measurements along the across-track direction with a spatial resolution that (in the cross-track direction) ranges between 43 km and 13 km with a spacing that ranges between 25 km and 12.5 km. The reconstruction problem is formulated according to (3) where $n = 64$ and $m = 1400$. This implies that the brightness field will be reconstructed on a finer resolution grid whose spacing is 1 km. The first set of experiments concerns simulated SSM/I-like measurements that are obtained through (3), approximating the integrated antenna pattern with a Gaussian function where the maximum gain is 43 dB [11], [32]. To simulate realistic measurements, a zero mean additive Gaussian noise with a standard deviation 1.06 K is used [8]. Both 1D profiles and a 2D brightness field are considered to test the performance of the proposed approach.
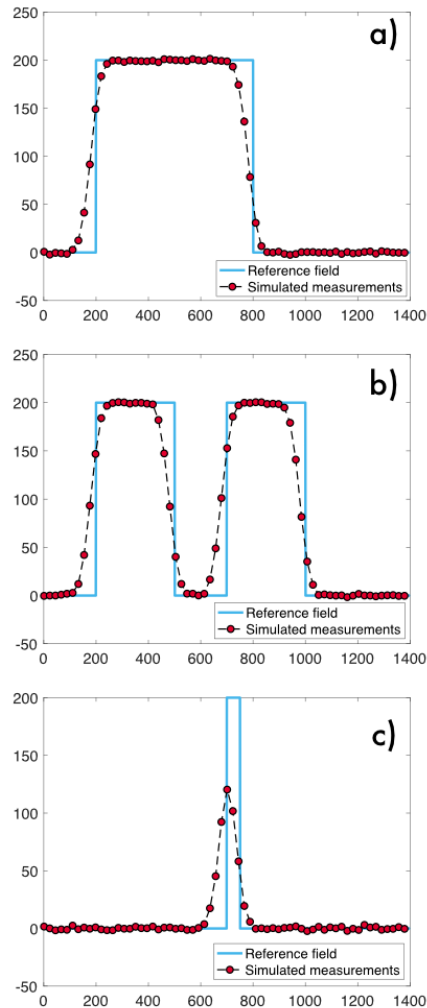
A. Simulations

Fig. 1. Simulated reference brightness field signals: (a) Rect $f_1(x)$, (b) Double Rect $f_2(x)$, (c) Spike $f_3(x)$. The red circles represent simulated noisy measurements.

With respect to the 1D case, three reference brightness profiles are simulated, which are shown in Fig. 1(a),(b),(c) (blue line):

$$f_1(x) = a \ \text{rect}\left(\frac{x - x_1}{\delta_1}\right)$$

$$f_2(x) = a \ \text{rect}\left(\frac{x - x_2}{\delta_2}\right) + a \ \text{rect}\left(\frac{x - x_3}{\delta_2}\right) \quad ,$$

$$f_3(x) = a \ \text{rect}\left(\frac{x - x_4}{\delta_3}\right)$$

(24)

where $a = 200$, $x_1 = 500$, $\delta_1 = 600$, $x_2 = 350$, $x_3 = 850$, $\delta_2 = 300$, $x_4 = 725$, $\delta_3 = 50$, and:

$$\text{rect}(t) = \begin{cases} 1 & |t| < 1 \\ 0 & |t| > 1 \end{cases} \quad . \quad (25)$$

The functions $f_1(x)$, $f_2(x)$ can be considered to model abrupt discontinuities which are related, for instance, to land/sea interface while $f_3(x)$ resembles small isolated islands. The simulated low-resolution noisy measurements are depicted in Fig.1(a),(b),(c) (red circles).
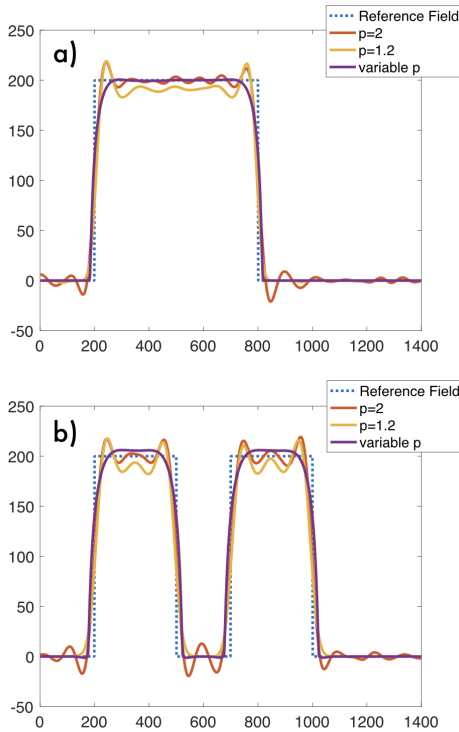

Fig. 2. Reference brightness profile (dotted blue line) and reconstructions at enhanced resolution obtained with gradient method in L^p with $p = 2$ (red line), $p = 1.2$ (yellow) and variable p (purple line) for: (a) rect-like signal (b) double rect-like signal.

The first experiment refers to the reference brightness profiles $f_1(x)$ and $f_2(x)$, see Fig. 1(a),(b). Reconstructions obtained using the variable p exponent method are

contrasted with reconstructions obtained using the fixed $p = 2$ and $p = 1.2$ exponent, see Fig. 2 (a),(b). The step size of the $p = 1.2$ and variable p exponent methods is empirically chosen and it is equal to 0.07 and 0.5, respectively.

All the methods result in a satisfactory reconstruction performance, since they provide reconstructions that well-fit the reference profile. As expected, $p = 2$ method (see red line) results in a reconstructed profile that presents Gibbs oscillations and a slight over-smoothness. Those drawbacks are mitigated by the $p = 1.2$ method (see yellow line) that results in a reconstructed profile where fluctuations are significantly reduced at the lower edges of the discontinuities. However, there are fictitious spikes at the upper edges of the discontinuities that call for significant overestimation of the brightness temperature by an amount of ~ 40 K. These spikes, which appear at both the sides of the discontinuity, represent a key drawback when dealing with the estimation of geophysical parameters from the resolution-enhanced measurements In addition, the mean level of T_B along the upper-part of the rect-like signal is not correctly reconstructed, showing an underestimation of around 50 K. Reconstructions obtained using the gradient method with the variable p exponent are shown in purple line. It can be noted that the method results in remarkable reconstructions where: a) the fictitious fluctuations (that appeared in the $p = 1.2$ reconstruction) disappeared; b) the upper-edge of the discontinuities is well-reconstructed (there is a small oscillation of about 5 K when dealing with the reference field $f_2(x)$), see Fig. 2(b); c) the abrupt discontinuity is very well reconstructed with the exception of the upper edges of the discontinuities that are over-smoothed with respect to both $p = 2$ and $p = 1.2$ reconstructions; d) no Gibbs-related oscillations appear.

The second experiment refers to the reference brightness profile $f_3(x)$, see Fig.1(c). Reconstructions (see Fig. 3) show that a remarkable performance is obtained by the $p = 2$ and $p = 1.2$ methods, with the $p = 1.2$ performing best in reconstructing the reference field profile without any Gibbs related oscillation. The variable p exponent method does not reconstruct correctly the reference profile since neither its amplitude nor its width are correctly reconstructed (see Fig. 3 in green line). This odd result is due to the choice of the step-size $\lambda = 0.5$. When a lower step-size is selected, i.e., $\lambda = 0.04$, a remarkable reconstruction is achieved, see Fig. 3 in purple line. In particular, the abrupt discontinuity is well-reconstructed and the upper side of the reference profile is well-reconstructed although slightly underestimated (~ 2 K). Note that, at the moment, no analytical formula is available to optimally select the step-size λ both in
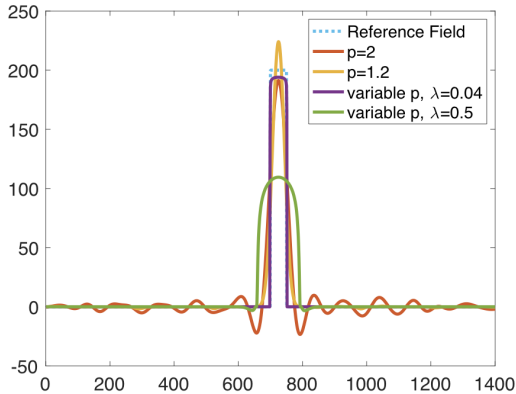
Fig. 3. Reference field (dotted blue line) and reconstructed field at enhanced resolution obtained with gradient method in L^p with $p = 2$ (red line), $p = 1.2$ (yellow) and variable p (purple line) using: step-size $\lambda = 0.5$ (green line) and step-size $\lambda = 0.04$ (purple line).
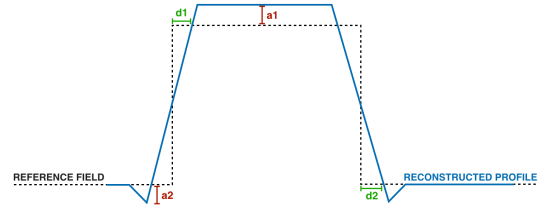

Fig. 4. Pictorial view of the 4 indices used to quantify the reconstructions performance with respect to the reference brightness profile.

the $p = 1.2$ and variable p cases. However, to check the robustness of the choice we made for the rect-like profile ($\lambda = 0.5$) and the spike-like profile ($\lambda = 0.04$), we made tailored experiments where we varied λ in the range [0.1,0.9] and [0.01,0.09] respectively. Results (not shown to save space) demonstrate that negligible differences apply in the reconstructed profiles as far as λ belongs to the above-mentioned ranges.

To quantitatively analyze the reconstructions performance, 4 indices are used to quantify the distance between the reconstructed and the reference profiles, see Fig. 4. In particular, $a1$ and $a2$ (whose reference value should be 0) refer to the reconstruction error with respect to the top of the edge and the background, respectively; while $d1$ and $d2$ (whose reference value should be 0 as well) refer to the reconstruction error with respect to the upper and lower-part of the discontinuity. Results related to the reconstructions obtained using L^2, $L^{1.2}$ and $L^{p(\cdot)}$ are listed in Table I for the three reference brightness profiles. Results show that the variable p exponent method performs best with all the indexes with the exception of $d1$. The latter witnesses that the $L^{p(\cdot)}$ method provides the worst result when the brightness profile $f_1(x)$ and $f_2(x)$ are used. This means that the $p = 2$ and $p = 1.2$ provide better reconstructions of the upper part of the discontinuity. However it must be noted that, as shown in Fig. 2 those methods fail in reconstructing the correct level of the brightness profile, resulting in an error that is around 20 K ($p = 1.2$) and 15 K ($p = 2$), respectively.

With respect to the 2D case the 1400×900 km simulated reference field is considered, see Fig. 5(a). It includes 10 targets that call for different dimensions

and brightness temperatures. It can be noted that some of the targets are very close to each other and they call for very similar brightness temperatures. Hence, this simulated scenario is very challenging. The simulated measurements field is shown in 5(b) where one can note that the low-pass filtering due to the band-limited radiometer transfer function, results in a coarse spatial resolution that, at once, limits the interpretability of the image. In fact, edges are blurred and some hot spots are not correctly detected. The field reconstructed at enhanced spatial resolution using the variable exponent p approach is shown in 5(c) where one can note that the edges of the larger target are very well reconstructed with negligible oscillations. In addition, the two pairs of close targets (on the rightmost-hand-side and on the upper-part of the image, respectively) are well resolved. The very small targets (whose size is approximately 10×20 km) are not visible in the reconstructed image. A deeper analysis on the reconstruction performance is undertaken contrasting reconstructions obtained using the proposed variable exponent p approach with the conventional $p = 2$ and $p = 1.2$ approaches in two different cases. The first case, shown in Fig. 5(d), refers to a transect that crosses the largest target (whose size is 200×200 km) along the along-track dimension. It can be noted that, even in this case, the variable p approach results in the best performance since it well fits both the sides of the discontinuity resulting in the lowest d_2 parameter. Moreover, it results in no oscillations at the lower edge of the discontinuity ($a_2 \simeq 0$) while it over-smoothes a little the upper edge of the discontinuity. The second case refers to a transect that crosses two targets which are very close to each other (~ 25 km in the along-scan direction), see Fig. 5(e). In this case, the targets are very small and no method succeeds in can accurate reconstruction pot the upper part of the hot spots that resembles Dirac-like delta functions. However, it can be noted that the variable p-exponent approach results in the best fitting of the abrupt discontinuity and results in no oscillations.

TABLE I
QUANTITATIVE ANALYSIS OF THE RECONSTRUCTION PERFORMANCE AGAINST THE REFERENCE BRIGHTNESS PROFILE.

	rect				double rect				spike			
	a1	a2	d1	d2	a1	a2	d1	d2	a1	a2	d1	d2
p = 2	12.1	22.9	28	26	17.2	17.1	28	27	9.3	19.9	-	25
p = 1.2	22.9	0	23	40	29.9	0	21	45	16	3.4	-	40
variable p	2.8	0	53	14	5.7	2.9	43	21	3.4	0	0	0
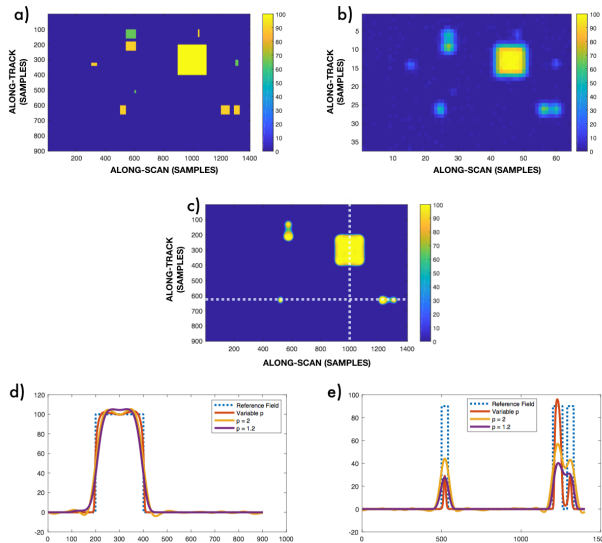
Fig. 5. (a) 2D reference brightness field where some discontinuities of different sizes and brightness temperatures are present. (b) Noisy simulated measurements obtained through (3) considering SSM/I parameters and a 1.09-K additive noise level. (c) Reconstructed field at enhanced resolution obtained with the variable p exponent method. (d) Brightness profile evolved according the along-track transect via the variable p, $p = 2$ and $p = 1.2$ reconstructed fields. (e) Brightness profile referred to the along-scan transect.

B. Real Data

Experiments undertaken on actual SSM/I measurements refer to five H-polarized brightness temperature fields collected in 1998 (day 278, F08 satellite) using the 19 GHz channel.

The third experiment concerns the brightness field measured over the Mediterranean sea, see Fig. 6 (a). A transect that includes portions of Spain, Baleari Islands, Sardinia and Italian peninsula is considered, see 6(b). It can be noted that the 1D extracted profile includes both rect-like and spot-like discontinuities that refers to land/sea transitions and small islands, respectively. The profiles reconstructed using the gradient method with $p = 2$, $p = 1.2$ and with variable p exponent are shown in Fig. 8(a) where the 19 GHz and 37 GHz non-enhanced fields, interpolated at the finer-resolution grid, are also
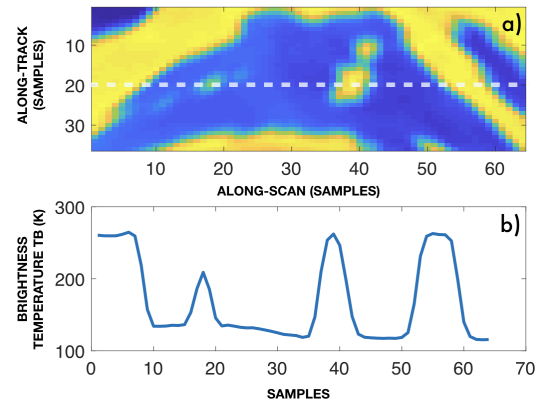

Fig. 6. (a) SSM/I 19.3 GHz H-polarized brightness temperature field. The white dotted line shows the along-scan transect selected for our study. (b) Brightness temperature profile related to the selected along-scan transect.
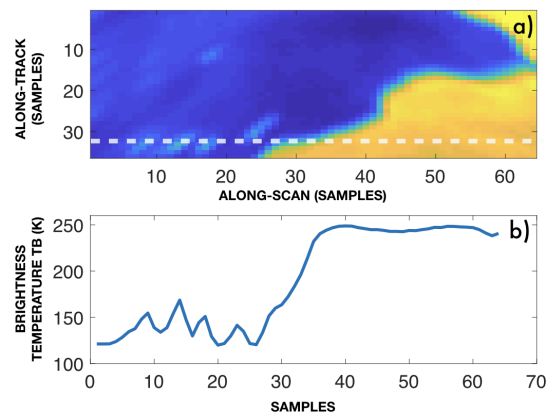

Fig. 7. (a) SSM/I 19.3 GHz H-polarized brightness temperature field. The white dotted line shows the along-scan transect selected for our study. (b) Brightness temperature profile related to the selected along-scan transect.

shown for reference purpose. Note that the latter channel is intrinsically characterized by a finer spatial resolution. All the methods provide satisfactory reconstruction performance since they result in a reconstructed profile that well-fits the reference profile resulting in better defined edges. It can be noted that the L^2 reconstruction suffers of Gibbs-related oscillations that are not visible when dealing with the $L^{1.2}$ reconstruction. However, they both exhibit significant oscillations in the upper-part of the edges. The best performance is provided by the variable p exponent method that results in a reconstruction that is not affected by neither Gibbs oscillations nor fluctuations over the top of the edges.

The fourth experiment concerns the brightness field related to a portion of the Atlantic Ocean, see Fig. 7 (a). A transect that includes the Canary Islands is considered, see 7 (b). It can be noted that the 1D extracted profile includes both rect-like and several spot-like discontinuities. The profiles reconstructed using the gradient method with $p = 2$, $p = 1.2$ and with variable p exponent are shown in Fig. 8(b) where the 19 GHz and 37 GHz non-enhanced fields, interpolated at the finer-resolution grid, are also shown for reference purpose. Again, all the methods provide satisfactory reconstructions, but the variabile p method provides the best result wiping out the oscillations on the land-portion of the L^2 and $L^{1.2}$ reconstructions.

The fifth experiment concerns three transects extracted from three different brightness fields (not shown to save space). The first one contains a portion of Tunisia and the islands of Sicily and Malta, see Fig. 9(a). The second one concerns the Bristol Bay, Alaska, and the transect (see Fig. 9(b) includes an isolated spike due to the presence of an isle. The third transect (see Fig. 9(c), extracted from a brightness field related to the central Africa, contains the Lake Victoria. The profiles reconstructed using the gradient method with $p = 2$, $p = 1.2$ and with variable p exponent are shown in Fig. 10(a),(b),(c) where the 19 GHz and 37 GHz non-enhanced fields, interpolated at the finer-resolution grid, are also shown for reference purpose. All the methods provide a satisfactory reconstruction performance since they result in a reconstructed profile that well-fits the reference profile. However it must be noted that L^2 reconstruction is strongly affected by Gibbs-related oscillations that are not visible when dealing with the $L^{1.2}$ reconstruction. Conversely, the $p = 1.2$ method results in fictitious oscillations that can be observed, for instance, in the top-part of the edge of Fig. 10(a) and over the area of Fig. 10(b). With respect to the the variable-p exponent method, it can be noted that it results in a reconstruction performance that significantly outperforms the $p = 2$ and $p = 1.2$ ones in the case of Fig. 10(a). The performance is significantly
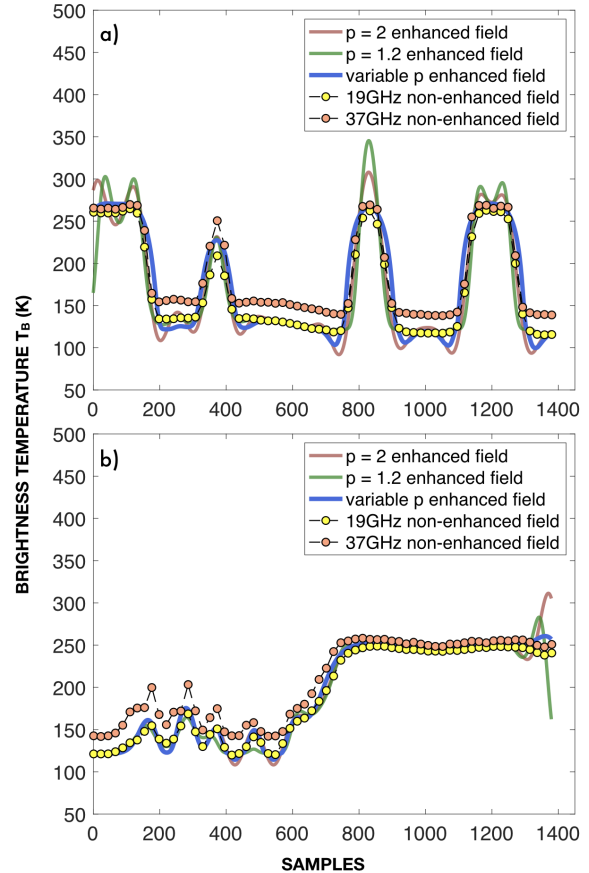

Fig. 8. Enhanced spatial resolution reconstructions obtained by L^p minimization approach with: p = 2 (red line), p = 1.2 (green line), variable p (blue line). The yellow and orange circles represent the 19 GHz and 37 GHz non-enhanced profiles, respectively. (a) Reconstructions related to the 1D transect of Fig. 5(b); (b) Reconstructions related to the 1D transect of Fig. 6(b).

(slightly) better than the $p = 2$ ($p = 1.2$) method in Fig. 10(b)-(c). Note that, in this case, the marginal improvement with respect to the $p = 1.2$ case is due to the presence of spot-like discontinuities that does not result in fictitious oscillations when the reconstruction is addressed in $p = 1.2$ Banach spaces.

CONCLUSIONS

A novel approach to enhance the spatial resolution of single-pass microwave radiometer measurements is proposed. The approach is mathematically based on the theory of regularization in Lebesgue spaces L^p with a variable p exponent. A reconstruction technique based on the gradient method is proposed that exploits a p exponent that varies in the range $[1.2, 2]$. The exponent is adaptively rescaled according to the characteristics of the non-enhanced brightness field in order to exploit the
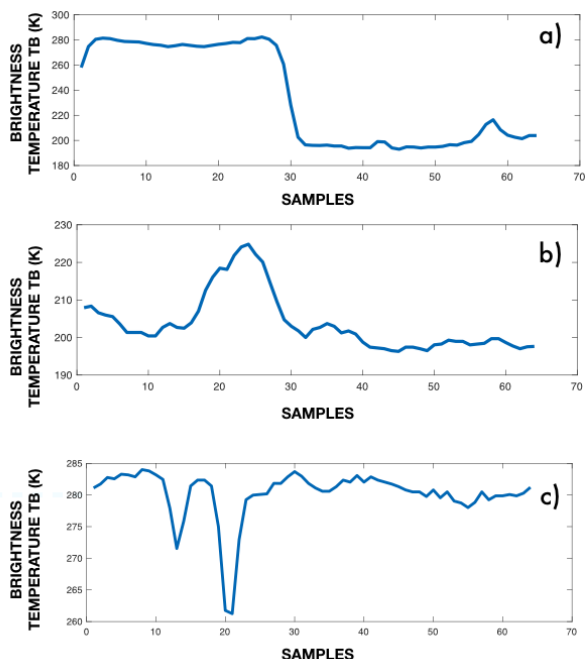
Fig. 9. Brightness temperature profile related to along-scan transects selected from SSM/I 19.3 GHz H-polarized brightness temperature field. The transects concern: (a) Tunisia and the island of Malta, (b) Bristol Bay area, Alaska, (c) Lake Victoria, Africa.

benefits of reconstructions in Hilbert and Banach spaces while mitigating their drawbacks. Experiments undertaken on both actual one-dimensional and simulated two-dimensional brightness profiles demonstrate the benefits of the proposed approach that reduces oscillations that characterize the L^2 and $L^{1.2}$ reconstructions while resulting in a comparable enhancement of the spatial resolution. Further developments will be devoted to the best tuning of the algorithm's parameters to reconstruct actual 2D brightness fields.

Fig. 10. Enhanced spatial resolution reconstructions obtained by L^p minimization approach with: p = 2 (red line), p = 1.2 (green line), variable p (blue line). The yellow and orange circles represent the 19 GHz and 37 GHz non-enhanced profiles, respectively. Reconstructions related to the brightness profile of: (a) Fig. 9(a), (b) Fig. 9(b) and (c) Fig. 9(c).

REFERENCES

[1] D. G. Long and M. J. Brodzik, "Optimum Image Formation for Spaceborne Microwave Radiometer Products," *IEEE Transactions on Geoscience and Remote Sensing*, vol. 54, no. 5, pp. 2763–2779, may 2016.
[2] J. Maslanik and J. Stroeve, "DMSP SSM/I-SSMIS Daily Polar Gridded Brightness Temperatures, Version 4," 2004.
[3] K. W. Knowles, E. J. Njoku, R. L. Armstrong and M. J. Brodzik, "Nimbus-7 SMMR Pathfinder Daily EASE-Grid Brightness Temperature," 2000.
[4] S. Sabaghy, J. Walker, L. Renzullo, and T. J. Jackson, "Spatially enhanced passive microwave derived soil moisture: Capabilities and opportunities," *Remote Sensing of Environment*, vol. 209, pp. 551–580, 2018.
[5] G. Poe, "Optimum interpolation of imaging microwave radiometer data," *IEEE Transactions on Geoscience and Remote Sensing*, vol. 28, no. 5, pp. 800–810, 1990.
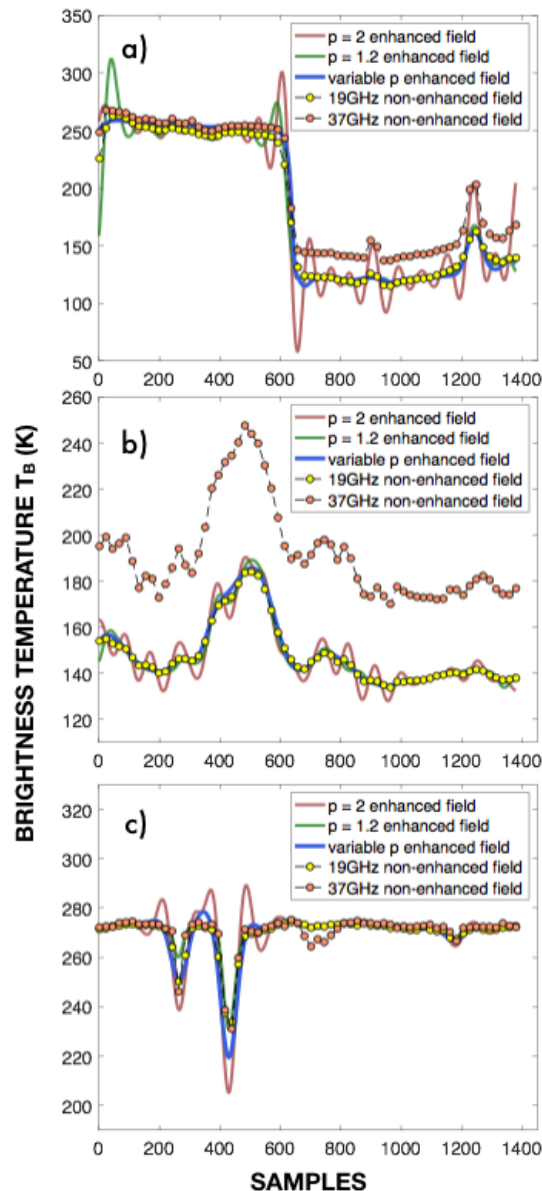[6] M. Farrar and E. Smith, "Spatial resolution enhancement of terrestrial features using deconvolved SSM/I microwave brightness temperatures," *IEEE Transactions on Geoscience and Remote Sensing*, vol. 30, no. 2, pp. 349–355, mar 1992.
[7] W. Robinson, C. Kummerow, and W. Olson, "A technique for enhancing and matching the resolution of microwave measurements from the SSM/I instrument," *IEEE Transactions on Geoscience and Remote Sensing*, vol. 30, no. 3, pp. 419–429, may 1992.

[8] D. G. Long and D. L. Daum, "Spatial resolution enhancement of SSM/I data," *IEEE Transactions on Geoscience and Remote Sensing*, vol. 36, no. 2, pp. 407–417, mar 1998.

[9] M. Migliaccio and A. Gambardella, "Microwave radiometer spatial resolution enhancement," *IEEE Transactions on Geoscience and Remote, Sensing*, vol. 43, 2005.

[10] A. Gambardella and M. Migliaccio, "On the Superresolution of Microwave Scanning Radiometer Measurements," *IEEE Geoscience and Remote Sensing Letters*, vol. 5, no. 4, pp. 796–800, oct 2008.

[11] F. Lenti, F. Nunziata, M. Migliaccio, and G. Rodriguez, "Two-Dimensional TSVD to Enhance the Spatial Resolution of Radiometer Data," *IEEE Transactions on Geoscience and Remote Sensing*, vol. 52, no. 5, pp. 2450–2458, 2014.

[12] M. Piles, D. Entekhabi, and A. Camps, "A Change Detection Algorithm for Retrieving High-Resolution Soil Moisture From SMAP Radar and Radiometer Observations," *IEEE Transactions on Geoscience and Remote Sensing*, vol. 47, no. 12, pp. 4125–4131, 2009.

[13] M. Choi and Y. Hur, "A microwave-optical/infrared disaggregation for improving spatial representation of soil moisture using AMSR-E and MODIS products," *Remote Sensing of Environment*, vol. 124, pp. 259–269, 2012.

[14] E. Santi, "An application of the SFIM technique to enhance the spatial resolution of spaceborne microwave radiometers," *International Journal of Remote Sensing*, vol. 31, no. 9, pp. 2419–2428, 2010.

[15] G. Backus and F. Gilbert, "Uniqueness in the Inversion of Inaccurate Gross Earth Data," *Philosophical Transactions of the Royal Society A: Mathematical, Physical and Engineering Sciences*, vol. 266, no. 1173, pp. 123–192, mar 1970.

[16] A. Stogryn, "Estimates of Brightness Temperatures from Scanning Radiometer Data," pp. 720–726, 1978.

[17] S. K. Chan *et al.*, "Development and assessment of the SMAP enhanced passive soil moisture product," *Remote Sensing of Environment*, vol. 204, pp. 931–941, 2018.

[18] D. G. Long and J. Stroeve, "Enhanced-Resolution SSM/I and AMSR-E Daily Polar Brightness Temperatures, Version 1," 2011.

[19] M. J. Brodzik and D. Long, "Calibrated Passive Microwave Daily EASE Grid 2.0 Brightness Temperature ESDR (CETB)," *NASA MEaSUREs*, 2015.

[20] F. Lenti, F. Nunziata, C. Estatico, and M. Migliaccio, "Spatial Resolution Enhancement of Earth Observation Products Using an Acceleration Technique for Iterative Methods," *IEEE Geoscience and Remote Sensing Letters*, vol. 12, no. 2, pp. 269–273, feb 2015.

[21] ——, "Analysis of Reconstructions Obtained Solving lp-Penalized Minimization Problems," *IEEE Transactions on Geoscience and Remote Sensing*, vol. 53, no. 9, pp. 4876–4886, sep 2015.

[22] T. Schuster, B. Kaltenbacher, B. Hofmann, and K. S. Kazimierski, *Regularization Methods in Banach Spaces*, ser. Radon series on computational and applied mathematics. De Gruyter, 2012.

[23] F. Lenti, F. Nunziata, C. Estatico, and M. Migliaccio, "On the Spatial Resolution Enhancement of Microwave Radiometer Data in Banach Spaces," *IEEE Transactions on Geoscience and Remote Sensing*, vol. 52, no. 3, pp. 1834–1842, mar 2014.

[24] ——, "Conjugate Gradient Method in Hilbert and Banach Spaces to Enhance the Spatial Resolution of Radiometer Data," *IEEE Transactions on Geoscience and Remote Sensing*, vol. 54, no. 1, pp. 397–406, 2016.

[25] B. A. Williams and D. G. Long, "Reconstruction From Aperture-Filtered Samples With Application to Scatterometer Image Reconstruction," *IEEE Transactions on Geoscience and Remote Sensing*, vol. 49, no. 5, pp. 1663–1676, 2011.

[26] M. Bertero and P. Boccacci, *Introduction to Inverse Problems in Imaging*. CRC Press, 1998.

[27] P. Brianzi, F. Di Benedetto, and C. Estatico, "Improvement of Space-Invariant Image Deblurring by Preconditioned Landweber Iterations," *SIAM Journal on Scientific Computing*, vol. 30, no. 3, pp. 1430–1458, 2008.

[28] F. Schöpfer, A. K. Louis, and T. Schuster, "Nonlinear iterative methods for linear ill-posed problems in Banach spaces," *Inverse Problems*, vol. 22, no. 1, pp. 311–329, feb 2006.

[29] C. Chidume, *Geometric properties of banach spaces and nonlinear iterations*. Springer-Verlag, 2009.

[30] L. Diening, P. Harjulehto, P. Hasto, and M. Ruzicka, *Lebesgue and Sobolev spaces with variable exponents*. Springer, 2011, vol. 2017.

[31] P. Matei, "A nonlinear eigenvalue problem for the generalized Laplacian on Sobolev spaces with variable exponent," *Romanian Journal of Mathematics and Computer Science*, vol. 2, pp. 70–82, 2012.

[32] J. P. Hollinger, J. L. Peirce, and G. A. Poe, "SSM/I instrument evaluation," *IEEE Transactions on Geoscience and Remote Sensing*, vol. 28, no. 5, pp. 781–790, 1990.